RSC Advances

PAPER

View Article Online
View Journal | View Issue

Cite this: *RSC Adv.*, 2026, **16**, 27202

Improving the performance of $FAPbI_3$ perovskite solar cells using a self-assembled monolayer

Mustafa Kareem, *[ab] Mustafa Abdullah,[c] Chetansinh R. Vaghela,[d] K. S. Kiran,[e] K. Parasuraman[f] and Sanjeev Kumar[g]

Received 30th March 2026
Accepted 7th May 2026

DOI: 10.1039/d6ra02657e

rsc.li/rsc-advances

In halide perovskite solar cells, the interfaces between the charge-transporting materials and perovskite significantly control the photovoltaic performance of the devices. In this simulation-based work, we introduce fullerene molecules as an interlayer between the front electrode and the perovskite layer to passivate surface defects and mitigate degradation arising from the direct contact between the electrode and the perovskite. Through SCAPS-1D simulation, we suggest that introducing a self-assembled monolayer reduces recombination losses, facilitates charge-carrier extraction, and improves band alignment in perovskite solar cells. We also evaluate the solar cell performance by tuning the perovskite layer thickness, trap-state density, shallow-acceptor density, parasitic resistances, and operating temperature to optimize the photovoltaic designs. The incorporation of this molecular modifier enables the simulation of conventional $FAPbI_3$-based perovskite solar cells with an efficiency of 24.07% under typical illumination conditions. Moreover, the optimized devices show high thermal stability, retaining 77% of their initial performance at 450 K.

1. Introduction

Renewable solar energy can provide a solution to the growing concern over global warming and atmospheric greenhouse pollutants from fossil fuels.[1,2] Therefore, the transition from fossil fuels to sustainable and green sources is a critical challenge that has attracted considerable attention.[3,4] Halide perovskite solar cells (HPSCs) have been widely investigated in recent years, with a verified power conversion efficiency (PCE) of 27%.[5] Organometallic $APbI_3$ perovskites utilizing formamidinium (FA^+) A-site cations have attracted significant attention owing to their promising optoelectronic characteristics.[6,7] The beneficial thermodynamic durability of the FA^+ cation makes α-$FAPbI_3$ more desirable for photovoltaic applications than methylammonium (MA^+)-based $APbI_3$ perovskites. Nevertheless, its spontaneous transformation to the yellow non-perovskite phase (δ-$FAPbI_3$) under ambient conditions poses an obstacle to its practical application.[8,9] The partial replacement of FA^+ with Cs^+ or MA^+ was shown to be an effective approach for stabilizing the α-phase of $FAPbI_3$ in ambient air, resulting in a narrower absorption spectrum and causing phase segregation.[10] Therefore, for the mass production of highly efficient HPSCs, the instability associated with phase conversion needs to be suppressed. Additionally, the presence of defects and dangling bonds at the perovskite interfaces induces a lattice mismatch, thus leading to interfacial stress. All these issues will substantially increase non-radiative recombination and impede efficient charge-carrier extraction.[11]

To address these issues, the self-assembled monolayer (SAM) method has been shown to be effective because of the generation of permanent dipole moments that adjust the band alignment, inhibit ion migration, passivate defects, and suppress recombination losses.[12,13] For $FAPbI_3$ perovskite, Cao *et al.* used [4-(3,6-dimethyl-9H-carbazol-9-yl)butyl] phosphonic acid as a SAM interlayer to engineer the interface between NiO_x and $FAPbI_3$. Me-4PACz enabled the passivation of interfacial defects and optimized the energetic alignment at the NiO_x/$FAPbI_3$ interface, thereby improving the charge collection.[14] Zhang *et al.* reported the etidronic acid SAM molecule at the buried interface of $FAPbI_3$ in the n–i–p HPSC architecture. This SAM layer could strongly bridge $FAPbI_3$ with the electron transport layer (ETL), thus stabilizing α-phase $FAPbI_3$ and reducing lead leakage in harsh environments.[15] In 2025, Xu *et al.* utilized a ferroelectric 1-adamantanamine hydroiodide SAM to tune the interfacial properties of HPSCs by creating a dipole layer over the $FAPbI_3$ film. The interfacial dipole

[a]College of Remote Sensing and Geophysics, Al-Karkh University of Science, Haifa St., Baghdad 10011, Iraq. E-mail: dr.mustafa@kus.edu.iq
[b]College of Science, University of Warith Al-Anbiyaa, 56001 Karbala, Iraq
[c]Electric Vehicles Engineering Department, Faculty of Engineering, Hourani Center for Applied Scientific Research, Al Ahliyya Amman University, Amman, Jordan
[d]Faculty of Science, Gokul Global University, Sidhpur, Gujarat, India
[e]Department of Physics, School of Engineering and Technology, JAIN (Deemed to Be University), Bangalore, Karnataka, India
[f]Department of Physics, Sathyabama Institute of Science and Technology, Chennai, Tamil Nadu, India
[g]Department of Physics, University Institute of Sciences, Chandigarh University, Mohali, Punjab, India

reduced energy-level misalignment and mitigated charge recombination; consequently, the HPSC yielded a PCE of 25.13%.[13] In this context, numerical simulations provide valuable insights into solar cell physics and can guide experimental efforts toward improved PCE and stability. A one-dimensional solar cell capacitance simulator (SCAPS-1D) is an extensively utilized software for the numerical simulation of solar cells. This tool allows for the examination of the photoelectric properties and carrier dynamics in HPSCs by resolving coupled Poisson and continuity equations under practical material and interface parameters.[16] Multiple SCAPS-1D investigations have designated the C_{60} interlayer as an efficient electron-selective material due to its advantageous band alignment and diminished interfacial recombination.[17] Song *et al.* improved the performance of inorganic $CsGeI_3$ HPSCs by incorporating a fullerene (C_{60}) interlayer using the SCAPS-1D tool. A (C_{60})-SAM formed a double electron transport structure, enhancing carrier transport and HPSC performance.[18]

In this simulation-based study using SCAPS-1D, we demonstrate that the incorporation of fullerene (C_{60}) as a self-assembled monolayer (C_{60}-SAM) underneath the $FAPbI_3$ perovskite layer significantly enhances the photovoltaic performance of HPSCs. Moreover, the C_{60} interlayer improves the interfacial band alignment due to the formation of a permanent dipole moment. The well-aligned energy levels between $FAPbI_3$ and C_{60} interlayer suppress the nonradiative carrier recombination and improve the fill factor (FF) and open circuit voltage (V_{OC}) of HPSCs. Consequently, a significant enhancement in the device performance of $FAPbI_3$ HPSC was realized, with the theoretical efficiency increasing from 7.5% to 24.07%. With this SAM treatment, only 23% degradation of HPSCs was observed at an elevated temperature (450 K) under AM 1.5 G illumination, predicting high thermal stability.

2. Methodology

The SCAPS-1D program was developed by Burgelman and his colleagues to model a variety of solar cells with up to seven layers.[19] The SCAPS-1D software operates based on the essential formulas of semiconductor physics, including the Poisson equation, continuity equations for electrons and holes, and drift-diffusion equations. The SCAPS-1D simulator is widely used for solar cell modeling since it provides direct calculations for the main photovoltaic parameters, simple implementation, and capability to add bulk and interfacial defect characteristics. The SCAPS-1 D tool can analyze significant device mechanisms, such as trap-assisted recombination, energy-level alignment, and interface properties, which are critical for understanding the role of C_{60} as an interlayer modifier. As an open-access program, SCAPS-1D enables researchers to define a wide range of input parameters, such as bandgap (E_g), dielectric constant (ε_r), carrier mobilities (μ), electron affinity (χ_e), doping densities, effective density of states, and trap-state densities (N_T), making it a practical resource for facilitating the advancement and assessment of novel photovoltaic designs.[20] In addition, typical carrier recombination methods, such as Auger processes, radiative recombination, and Shockley–Read–Hall (SRH) recombination by bulk traps, are included.

The typical AM 1.5 G solar irradiation with an intensity of 1000 W m^{-2} at a temperature of 300 K was employed as the input illumination for the device simulation. We utilized fluorine-doped tin oxide (FTO) as an illuminated side with a flat-band contact, while gold (Au) was used as a back contact. It is found that SCAPS-1D calculations can be aligned with the experimental results when critical conditions, such as parasitic resistances and interfacial and bulk defects, are taken into account. We set the series resistance (R_S) and shunt resistance (R_{SH}) to 4 ohm cm^2 and 500 ohm cm^2, respectively. As depicted in Table S1, interfacial layers with $N_{Trap} = 1.02 \times 10^{12}$ cm^{-2} were added at the ETL/$FAPbI_3$ and $FAPbI_3$/HTL interfaces. Unfortunately, time-dependent degradation processes, such as chemical changes, thermal aging, and ionic migration, cannot be conducted using SCAPS-1D because it operates under steady-state conditions.

3. Results and discussion

We examined the initial photovoltaic performance of the HPSCs using the input parameters shown in Table 1. $FAPbI_3$-based HPSC was simulated utilizing the configuration illustrated in Fig. 1a. Fig. 1b and c show the band structure diagram of the ordered layers in the equilibrium-simulated HPSC. The FTO/C_{60}/$FAPbI_3$/spiro-OMeTAD/Au stack exhibited a preferable energy-level alignment with small band offsets, promoting charge-carrier extraction from $FAPbI_3$ toward the respective electrodes. Additionally, Fig. S1 demonstrates a strong built-in potential (V_{bi}) at the C_{60}/$FAPbI_3$ interface, providing a driving force for electrons. Fig. 1d depicts the absorption coefficient (α) profiles for the HPSC layers extracted from the default SCAPS-1D. The $FAPbI_3$ perovskite exhibited the highest absorption, while the ETL and HTL exhibited low absorption, operating as light window layers. Fig. 1e shows the current density–voltage (J–V) characteristics of the reference HPSC under AM 1.5 G solar light. The reference device had a PCE of 18.25% with a short circuit current (J_{SC}) of 24.46 mA cm^{-2}, V_{OC} of 1.04 V, and fill factor (FF) of 71.08%. The incident photon-to-current efficiency (IPCE) spectrum (Fig. 1f) was calculated to verify the high J_{SC} value. The IPCE of the reference device was high over the entire visible-light absorption region, indicating efficient photon harvesting and charge-carrier separation/transportation.[27]

Normally, defects in perovskite layers generate energy states that operate as nonradiative recombination sites, which result from undercoordinated species, impurity inclusion, or lattice disorder, especially under poorly controlled fabrication conditions, which severely deteriorate HPSC performance. The effect of perovskite trap-state density (N_{Trap}) on the photovoltaic properties of HPSCs was analyzed by varying N_{Trap} from 10^{15} cm^{-3} to 10^{19} cm^{-3} (Fig. 2a). Deep-level traps significantly reduce carrier lifetimes and diffusion lengths through SRH recombination.[28] As N_{Trap} increased, all parameters decreased significantly. J_{SC} decreased from 24.46 mA cm^{-2} at 10^{15} cm^{-3} to 4.26 mA cm^{-2} at 10^{19} cm^{-3} (Fig. 2b), which was attributed to the increased SRH processes at the recombination sites (Fig. 2f),

Table 1 Key parameters of the layers used in the HPSC structure

Parameters (units)	C_{60}-SAM	$FAPbI_3$	Spiro-OMeTAD
Thickness [nm]	3.0	550	200
Bandgap [eV]	2.3	1.53	3.01
Electron affinity [eV]	4.0	4.0	2.18
Dielectric permittivity	4.4	25	3
Effective density of states in conduction band [cm^{-3}]	1.0×10^{18}	1.8×10^{19}	2.2×10^{18}
Effective density of states in valence band [cm^{-3}]	1.8×10^{19}	2.2×10^{18}	2.0×10^{17}
Electron mobility [$cm^2\ V^{-1}\ s^{-1}$]	3.8×10^{-3}	27	7.9×10^{-3}
Hole mobility [$cm^2\ V^{-1}\ s^{-1}$]	1.0×10^{-5}	27	7.9×10^{-3}
Electron thermal velocity [$cm\ s^{-1}$]	1.0×10^{7}	1.0×10^{7}	1.0×10^{7}
Hole thermal velocity [$cm\ s^{-1}$]	1.0×10^{7}	1.0×10^{7}	1.0×10^{7}
Shallow-donor density [cm^{-3}]	1.0×10^{18}	—	—
Shallow-acceptor density [cm^{-3}]	—	1.0×10^{15}	1.2×10^{17}
Defect type	Neutral	Neutral	Neutral
Trap-state density [cm^{-3}]	1.0×10^{16}	1.8×10^{15}	1.0×10^{15}
Electron-capture cross-section [cm^2]	1.0×10^{-15}	1.0×10^{-15}	1.0×10^{-15}
Hole-capture cross-section [cm^2]	1.0×10^{-15}	1.0×10^{-15}	1.0×10^{-15}
Defect position above the valence-band edge [eV]	0.6	0.6	0.6
Energetic distribution	Single	Single	Single
References	21	22 and 23	24–26

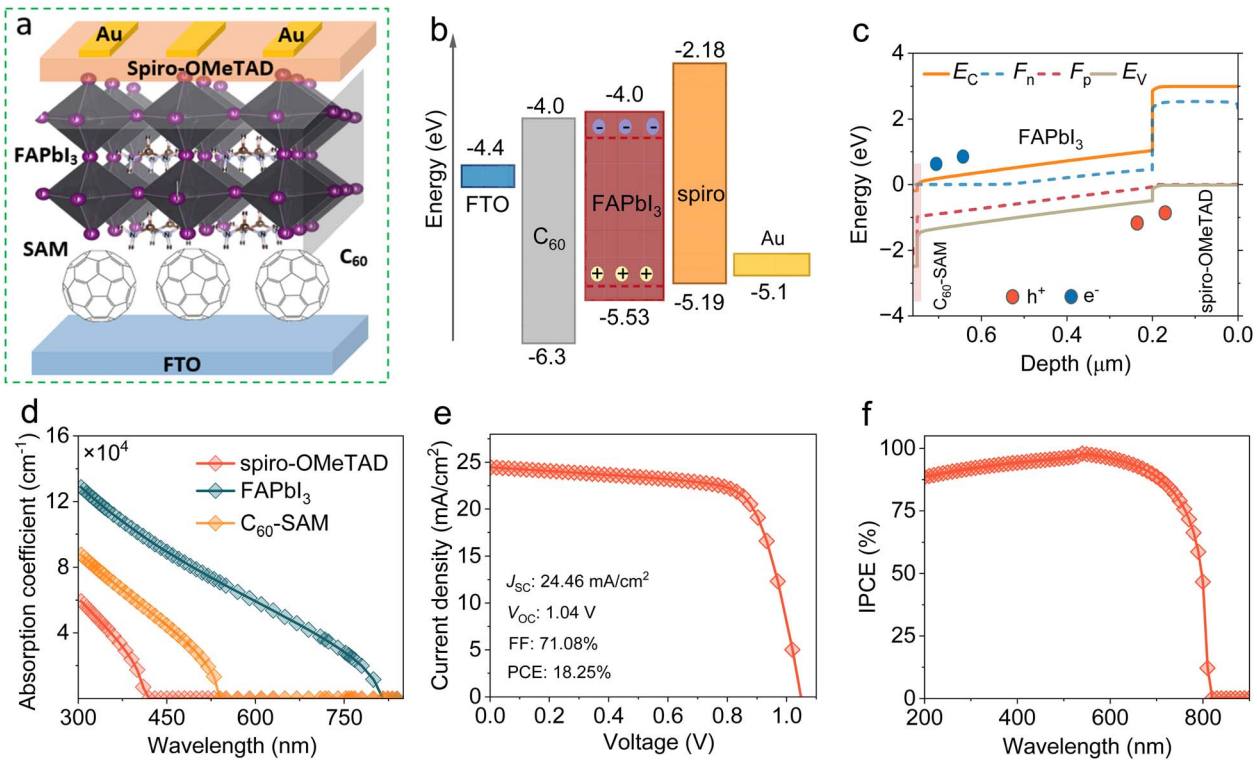

Fig. 1 Initial simulation and schematic of HPSC with C_{60}. (a) Configuration of a typical HPSC. (b) Energy level alignment. (c) Band structure diagram of C_{60}/$FAPbI_3$/spiro-OMeTAD. (d) Absorption coefficient plots. (e) *J*–*V* curve of the simulated device under AM1.5 illumination. (f) IPCE response.

leading to a reduction in carrier diffusion lengths from 2.6 μm to 26 nm. Furthermore, the decrease in J_{SC} can be attributed to the inhibited photocarrier generation, as confirmed by the reduced IPCE spectrum, as depicted in Fig. 2d. The V_{OC} also shows a decreasing pattern with N_{Trap}. As stated in the diode equation $\left(V_{OC} = \frac{KT}{q}\ln\left(\frac{J_{SC}}{J_o} + 1\right)\right)$,[29] an enhanced recombination rate at higher defect levels causes an increase in the reverse saturation current (J_o), thus limiting V_{OC}. FF in Fig. 2c also decreases with increasing N_{Trap} due to the reduced recombination resistance (R_{rec}), which is consistent with the impedance analysis (Fig. 2e). Nyquist plots exhibit a shrinkage in the semi-circular curve with increasing N_{Trap}, indicating R_{rec} suppression in the HPSC devices. The PCE results demonstrate

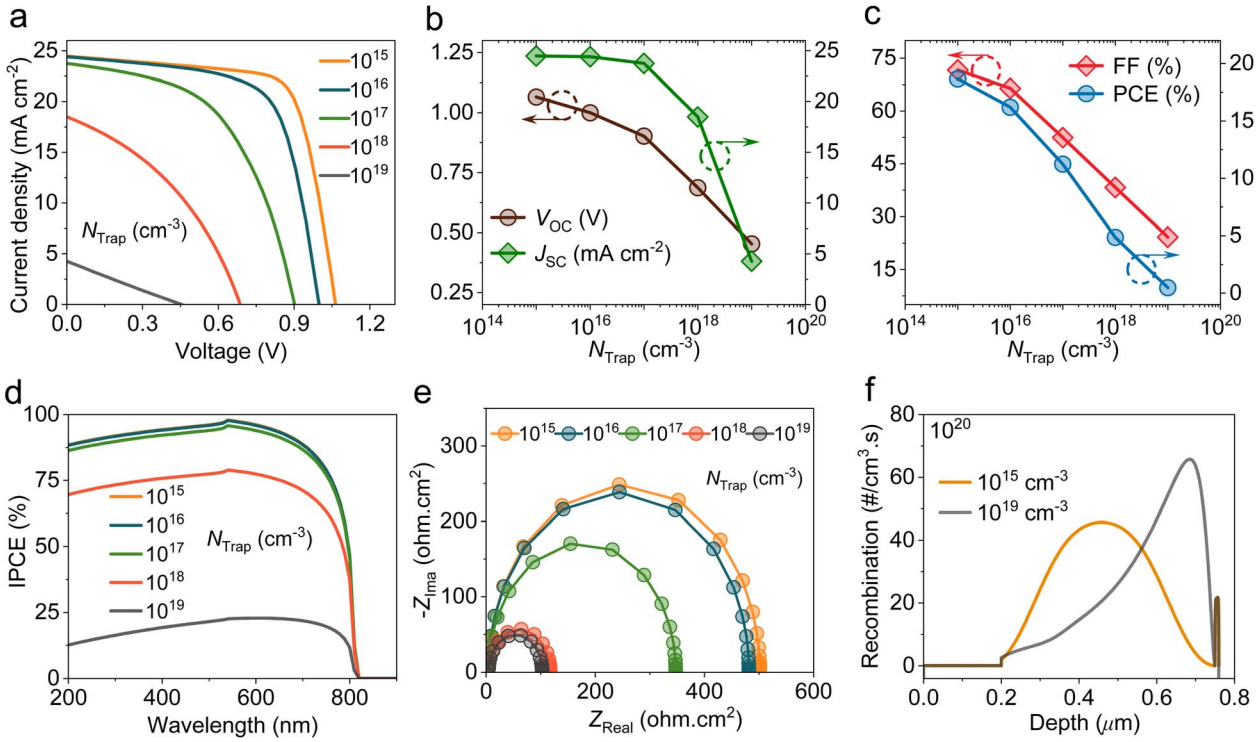

Fig. 2 Analysis of the impact of the trap-state density within $FAPbI_3$ on the performance of HPSCs. (a) J–V characteristics. (b) Dependency of V_{OC} and J_{SC} on N_{Trap}. (c) Variations in FF and PCE with N_{Trap}. (d) IPCE spectra. (e) Nyquist plots derived from the impedance measurements. (f) Recombination rates at low and high N_{Trap} concentrations.

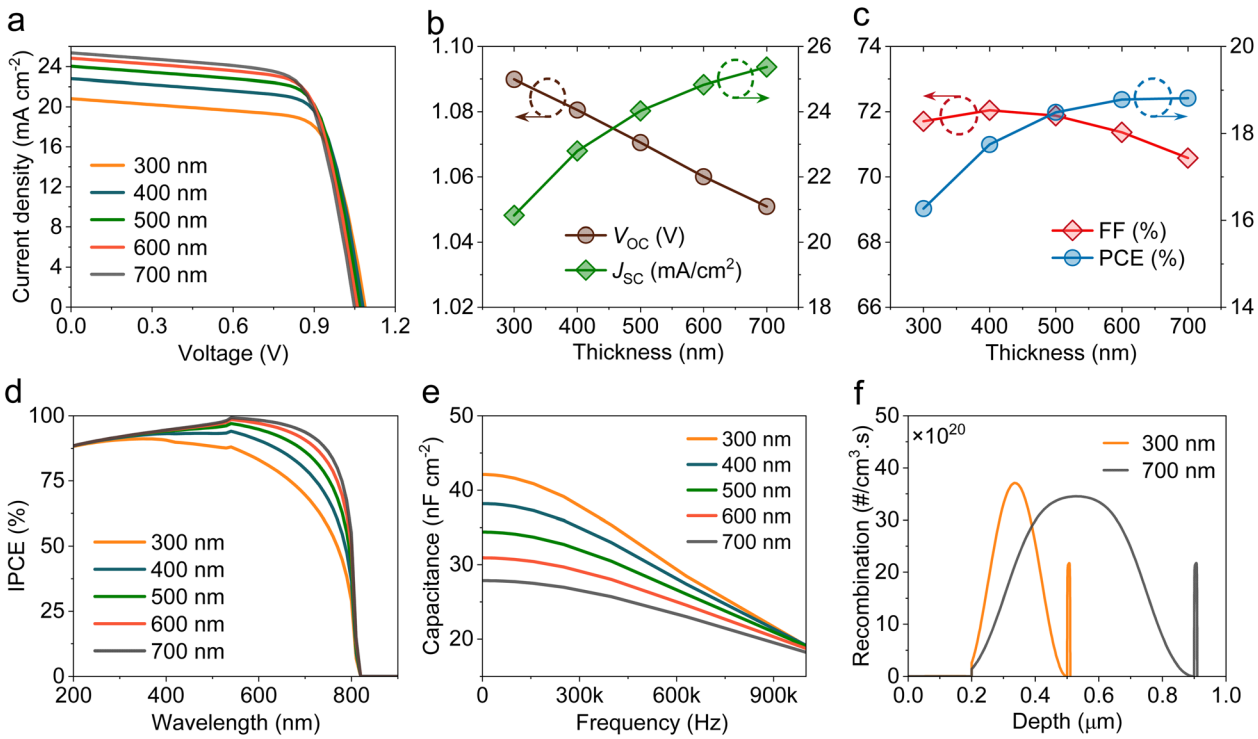

Fig. 3 Impact of the $FAPbI_3$ absorber thickness on the performance of HPSCs. (a) J–V curves. (b) Variations in V_{OC} and J_{SC}. (c) Evaluations of FF and PCE. (d) IPCE spectra. (e) C–f plots under AC perturbation. (f) Recombination rate profiles at 300 nm and 700 nm thicknesses.

a pronounced decrease from 18.67% to 0.46% with increasing N_{Trap}, underscoring the need for deep-level defect management.

The effect of $FAPbI_3$ thickness on the photovoltaic parameters of C_{60}-based HPSCs was investigated by varying the perovskite thickness in the range of 300 nm to 700 nm (Fig. 3a). As depicted in Fig. 3b, the optimum J_{SC} value is obtained for thicknesses of around 600 to 700 nm. Increasing the perovskite thickness improves J_{SC} due to the increased IPCE across a wider spectral range caused by enhanced light harvesting in the longer wavelength region, as shown in Fig. 3d. Conversely, V_{OC} exhibited a decreasing trend with increasing perovskite thickness because of the spreading of V_{bi} across a longer region, limiting drift efficiency. FF (Fig. 3c) slightly decreases with increasing perovskite thickness mainly due to the higher R_S and trap-mediated recombination in thicker perovskites, as depicted in Fig. 3f. The 700 nm $FAPbI_3$ layer shows a wider distribution of recombination rates, which leads to an increase in carrier pathways, thereby increasing the probability of recombination. Collectively, the PCE improved with the $FAPbI_3$ thickness, and the optimum device with 700 nm yielded a V_{OC} of 1.05 V, a J_{SC} of 25.36 mA cm^{-2}, an FF of 70.57%, and a PCE of 18.81%. Finally, Fig. 3e illustrates the capacitance–frequency (*C–f*) curves of HPSCs with different perovskite thicknesses. Thick absorbers showed lower capacitance due to reduced interfacial carrier aggregation and a weaker depletion region at the interfaces.[30] Additionally, we note that the capacitance of HPSC decreases as frequency increases due to slow ionic and polarization processes, indicating a weaker internal electric field.

Fig. 4a illustrates the *J–V* plots of HPSCs with the shallow acceptor density (N_A) changing from 10^{14} to 10^{18} cm^{-3}. From Fig. 4b, it is evident that the V_{OC} increases from 1.05 to 1.18 V as N_A increases from 10^{14} to 10^{18} cm^{-3}. Meanwhile, there is only a slight reduction in the J_{SC} values with an increase in N_A levels. The enhancement in N_A level boosted V_{bi} and reduced saturation current density, which enhanced quasi-Fermi level splitting (QFLS) and thus increased V_{OC}. Moreover, a slight reduction in J_{SC} parameter is due to increased SRH recombination processes, which lead to shortening carrier lifetime, thus minimizing carrier separation. As shown in Fig. 4c, it is clear that FF increases from 71.19% to 73.53% and PCE increases from 19.08% to 21.29% with increasing N_A value. The J_{SC} reduction is attributed to increased interfacial recombination losses that suppressed optical absorption efficiency, as confirmed by the IPCE results in Fig. S2. The V_{OC} improvement can be explained using the band diagram structure depicted in Fig. 4d and e. With increasing N_A doping, band bending and internal V_{bi} are improved. These improvements lead to a significant increase in QFLS. Additionally, the suppressed recombination rate (Fig. 4f) in the perovskite layer lowers J_o, thus enhancing V_{OC}.

A low R_S assists effective charge-carrier extraction, suppresses power losses, and optimizes the overall performance of the HPSC. This can be realized by tuning materials and interfaces and designing the cell structure. Fig. 5a presents the evaluation of the *J–V* curves of HPSCs with varying R_S in the

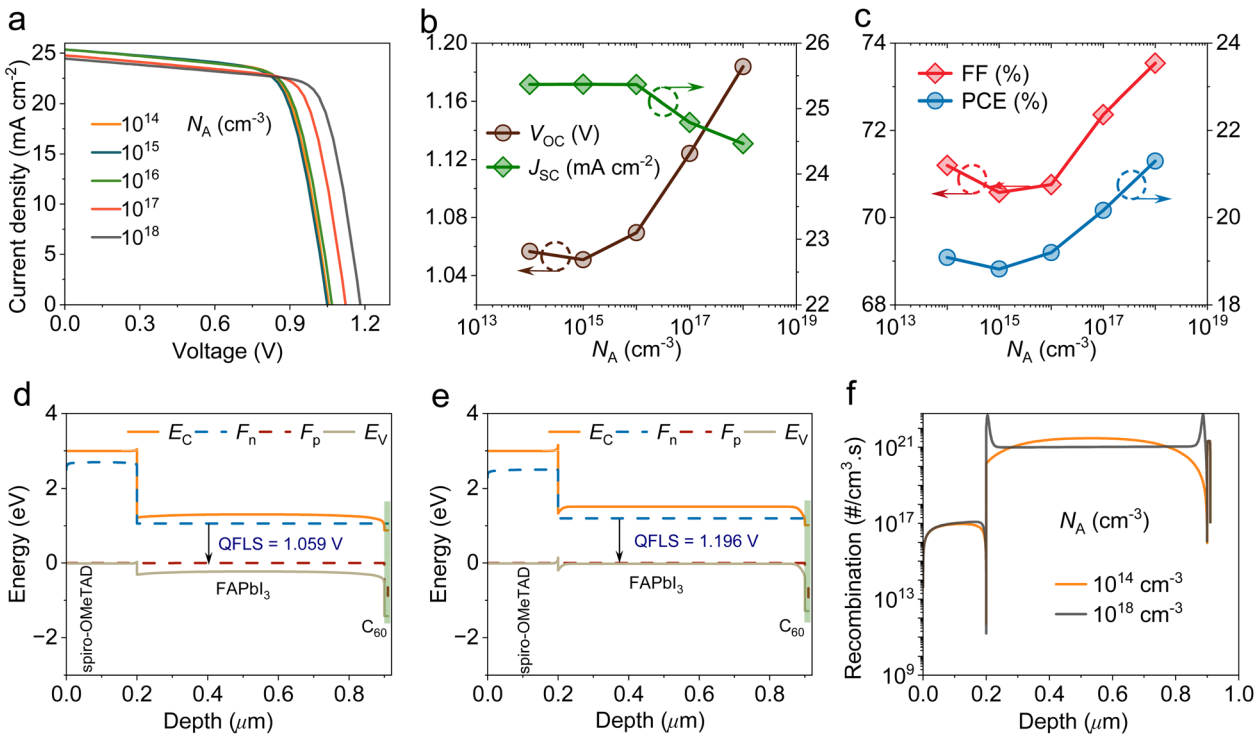

Fig. 4 Effect of the $FAPbI_3$ acceptor density on the performance of HPSCs. (a) *J–V* curves. (b) Variations in V_{OC} and J_{SC}. (c) Evaluations of FF and PCE. (d) Band diagram structure of HPSC with 10^{14} cm^{-3} acceptor density. (e) Band diagram structure of HPSC with a 10^{18} cm^{-3} acceptor density. (f) Recombination rate profiles at 10^{14} cm^{-3} and 10^{18} cm^{-3} acceptor densities.

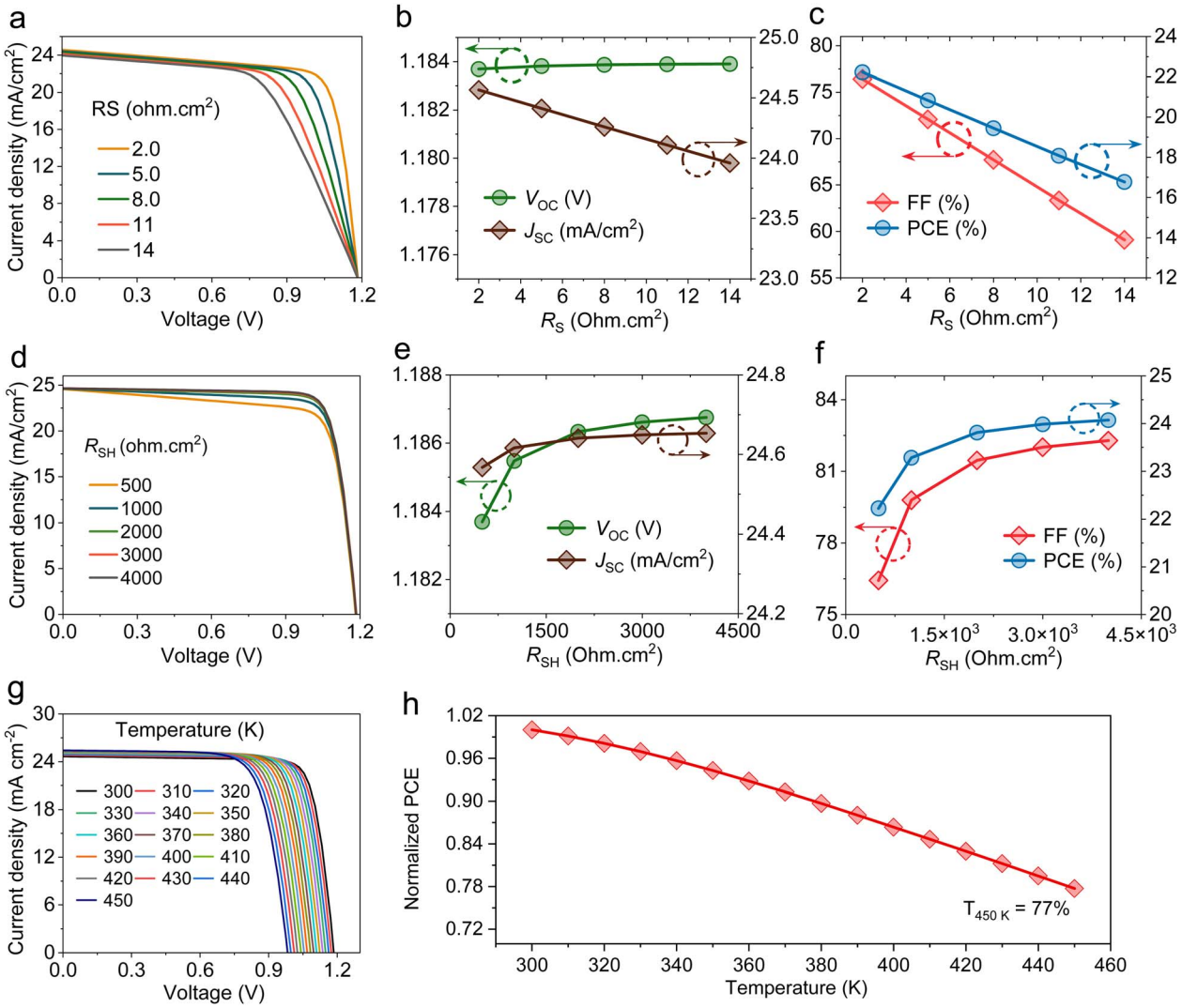

Fig. 5 Analysis of resistive losses and operating temperature on HPSC performance. (a) J–V characteristics with varying R_S. (b) Variations in V_{OC} and J_{SC}. (c) Evaluations of FF and PCE. (d) J–V plots with changing R_{SH}. (e) Variations in V_{OC} and J_{SC}. (f) Evaluations of FF and PCE. (g) J–V plots at different temperatures. (h) Normalized PCEs.

range of 2 to 14 ohm cm^2. As illustrated in Fig. 5b, J_{SC} decreases as R_S increases from 24.56 mA cm^{-2} to 23.95 mA cm^{-2} due to increased resistive losses in the cell that impede charge generation and collection.[31] V_{OC} reveals negligible changes with varying R_S, as it mostly relies on recombination, making it less sensitive to R_S changes. Variations in R_S exhibited the most significant effect on FF, which reduced from 76.42% to 59.09% (Fig. 5c). The increased internal resistive losses deform the J–V plots, which decrease the maximum power and result in FF deterioration. Therefore, PCE decreases sharply from 22.22% to 16.76% with increasing R_S.

Optimizing R_{SH} suppresses undesirable leakage current pathways within the HPSC, boosting device performance. Fig. 5d presents the impact of R_{SH} on the performance of HPSCs with a fixed R_S at 2 ohm cm^2. J_{SC} remained relatively constant with increasing R_{SH}, while V_{OC} improved gradually as R_{SH} increased from 500 to 4000 ohm cm^2 (Fig. 5e). As shown in Fig. 5f, a gradual enhancement in FF is observed, as R_{SH} is in the range of 500–3000 ohm cm^2, beyond which it becomes constant. Consequently, PCE follows the same pattern as FF; it increases by 24.07% at 4000 ohm cm^2. The Nyquist plots shown in Fig. S3 can explain this improvement. At high R_{SH}, leakage routes are suppressed; thus, fewer photocarriers are lost, leading to improved R_{rec}, as reflected by a larger semicircle diameter in the Nyquist plots.

The experimental reports state that the main challenge of HPSCs is their long-term durability. Therefore, it is important to investigate the effect of operating temperature on the efficiency of C_{60}-based HPSCs. Fig. 5g depicts that J_{SC} shows a minor enhancement from 24.653 mA cm^{-2} to 25.421 mA cm^{-2} with rising operating temperatures. This J_{SC} improvement is attributed to the energy bandgap narrowing of perovskite, resulting in higher photon harvesting and improved charge carrier mobility.[32] V_{OC} and FF were strongly affected by higher temperatures, consistent with previous studies.[33] V_{OC} is one of the main parameters influenced by increasing temperatures, as

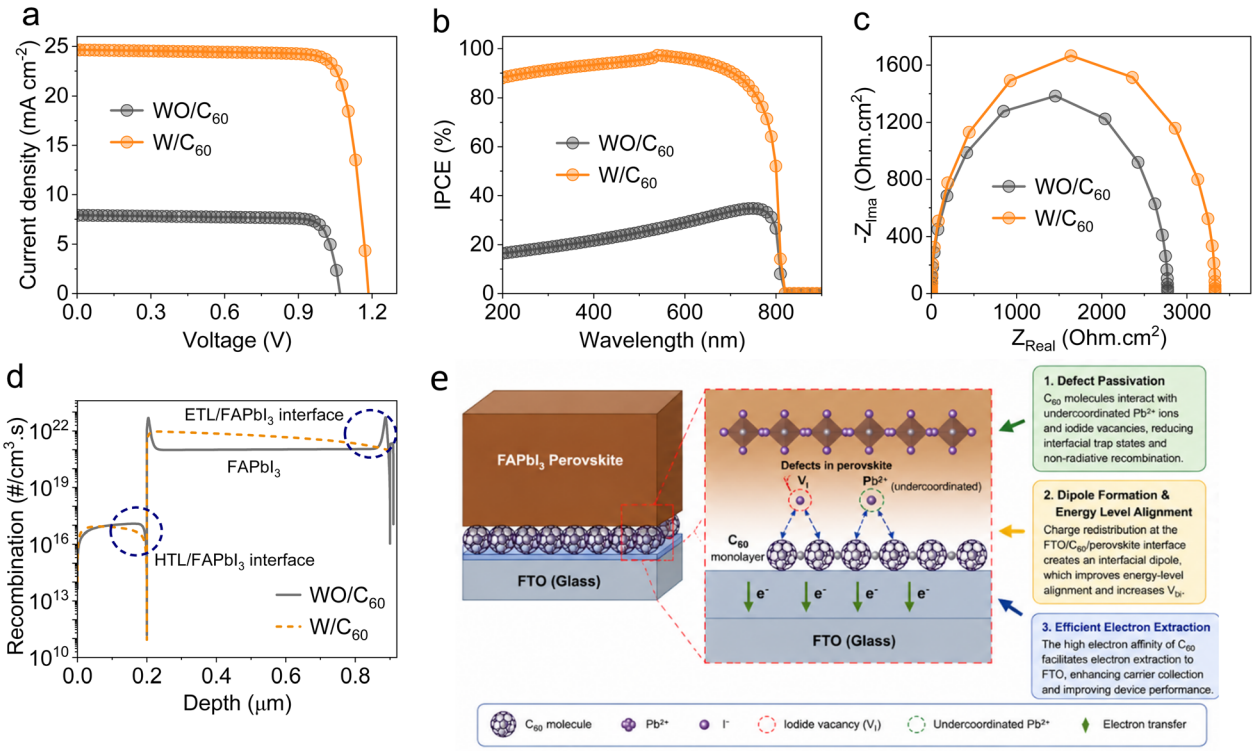

Fig. 6 Effect of the C_{60} self-assembled monolayer on photocurrent performance and interfacial charge dynamics in HPSCs. (a) *J*–*V* curves. (b) IPCE spectra. (c) Nyquist plots. (d) Recombination rate profiles. (e) Proposed mechanism for defect passivation using the C_{60} self-assembled monolayer molecule.

they are closely associated with J_o. Increased device temperature increases charge thermal energy, which leads to higher non-radiative recombination rates, thus limiting V_{OC} and FF. Both V_{OC} and FF decreased from 1.186 V to 0.983 V and 82.284% to 74.824% with an increasing operating temperature from 300 K to 450 K, respectively, thereby declining cell efficiency.[34,35] Based on the simulation calculations (Fig. 5h), the devices showed good thermal stability, maintaining 77% of their initial performance at 450 K.

Introducing C_{60} interlayer at the electrode/perovskite interface can improve electronic quality and electron collection efficacy of the $FAPbI_3$-based HPSCs. The C_{60} layer can passivate Pb^{2+} and iodide vacancy defects, thus suppressing recombination losses. Therefore, a device with C_{60} showed higher photoconversion performance, as confirmed by the improved *J*–*V* plot (Fig. 6a) and IPCE spectrum (Fig. 6b). Moreover, Nyquist analysis exhibits higher recombination resistance for the device with C_{60}, as illustrated in Fig. 6c, implying suppressed carrier recombination. Fig. 6d shows a clear reduction in the recombination rate at the ETL/$FAPbI_3$ and $FAPbI_3$/HTL interfaces, further confirming the role of SAM in suppressing SRH recombination pathways. The optimized HPSC achieved a PCE of 24.07% with a J_{SC} of 24.65 mA cm^{-2}, a V_{OC} of 1.186 V, and an FF of 82.28%.

The C_{60} modifier could introduce a uniform interfacial layer between the conductive oxide substrate and perovskite absorber *via* van der Waals interactions even without anchoring functional groups. As shown in Fig. 6e, this interlayer could induce a passivation effect by interacting with undercoordinated Pb^{2+} ions and iodide vacancies, thus reducing non-radiative recombination rates.[36] Furthermore, the C_{60} interlayer could improve the interfacial energy level alignment due to the formation of

Table 2 A summary comparison of the obtained device parameters with the reported $FAPbI_3$-based HPSCs[a]

Author	Structure	V_{OC} (V)	J_{SC} (mA cm^{-2})	FF (%)	PCE (%)
Kumar *et al.*[40]	FTO/SnO_2/$FAPbI_3$/spiro-OMeTAD/Au	1.115	24.54	76.93	21.72
Anjan *et al.*[41]	FTO/c-TiO_2/mp-TiO_2/$FAPbI_3$/spiro-OMeTAD/Au	1.155	25.24	82.89	24.16
Jeong *et al.*[8]	FTO/c-TiO_2/mp-TiO_2/$FAPbI_3$/OAI/spiro-OMeTAD/Au	1.189	26.35	81.70	25.60
Meng *et al.*[42]	ITO/SnO_2/$FAPbI_3$/spiro-OMeTAD/Au	1.188	26.22	81.38	25.36
Du *et al.*[43]	FTO/TiO_2/$FAPbI_3$/PEAI/spiro-OMeTAD/Au	—	—	—	24.00
Xiong *et al.*[44]	FTO/SnO_2/$FAPbI_3$/spiro-OMeTAD/MoO_3/Ag	1.130	25.37	80.90	23.19
This work	**FTO/C_{60}/$FAPbI_3$/spiro-OMeTAD/Au**	**1.186**	**24.65**	**82.28**	**24.07**

[a] OAI: octylammonium iodide; mp-TiO_2: mesoporous titanium dioxide; MoO_3: molybdenum trioxide; and PEAI: phenethylammonium iodide.

a permanent dipole moment, which facilitates electron extraction.[37] Density functional theory calculations reveal that the C_{60} interlayer could interact with $MAPbI_3$ perovskite by generating interfacial charge redistribution and modulating surface energy, thereby enhancing charge transport.[38] Finally, the C_{60} interlayer could significantly reduce the *J–V* hysteresis of HPSCs by passivating the localized and accumulated ions, which act as trap-assisted carrier recombination sites in HPSCs, resulting in large *J–V* hysteresis.[39]

Table 2 compares the photovoltaic parameters of the simulated HPSCs with the experimentally reported $FAPbI_3$-based devices. The obtained parameters are consistent with those of previous studies, confirming the validity of the adopted material parameters and simulation process as well as capturing accurate carrier dynamics in HPSCs.

4. Conclusion

In summary, we reported a substantial efficiency enhancement of $FAPbI_3$ solar cells from 7.5% to 24.07% by incorporating a self-assembled monolayer of fullerene (C_{60}) between the FTO electrode and the $FAPbI_3$ perovskite. The insertion of the C_{60} interlayer led to enhanced energetic band alignment, reduced charge recombination, and improved charge extraction–transportation capabilities. All these factors contributed to the surge in the photovoltaic parameters. Impedance analysis confirms a significant reduction in trap-assisted recombination using the C_{60} modification. Furthermore, the addition of C_{60} interlayer enhanced the high-temperature stability. The SCAPS-1D simulation further confirms the importance of perovskite layer optimization for designing efficient and stable HPSCs. Perovskite optimization was accomplished by tuning the perovskite thickness, trap-state density, and shallow acceptor concentration. Our simulation results offer useful guidance for the ongoing optimization of fabrication processes in high-efficiency $FAPbI_3$-based HPSCs.

Author contributions

Mustafa Kareem: formal analysis; conceptualization; methodology; writing – original draft; writing – review & editing, validation. Mustafa Abdullah: methodology; conceptualization; writing – original draft. Chetansinh R. Vaghela: writing – original draft; writing – review & editing. Kiran K. S.: software; formal analysis; writing – review & editing. Parasuraman K.: writing – original draft; methodology; software. Sanjeev Kumar: investigation; writing – review & editing; supervision.

Conflicts of interest

The authors declare no conflicts of interest.

Data availability

The data will be available from the corresponding author on reasonable request.

Supplementary information (SI) is available. See DOI: https://doi.org/10.1039/d6ra02657e.

References

1 H. Togun, A. Basem, M. J. Jweeg, N. Biswas, A. M. Abed, D. Paul, H. I. Mohammed, A. Chattopadhyay, B. K. Sharma and T. Abdulrazzaq, Advancing organic photovoltaic cells for a sustainable future: The role of artificial intelligence (AI) and deep learning (DL) in enhancing performance and innovation, *Sol. Energy*, 2025, **291**, 113378.
2 H. Togun, A. Basem, A. A. H. Kadhum, A. M. Abed, N. Biswas, F. L. Rashid, R. A. Lawag, H. M. Ali, H. I. Mohammed and D. K. Mandal, Advancing photovoltaic thermal (PV/T) systems: Innovative cooling technique, thermal management, and future prospects, *Sol. Energy*, 2025, **291**, 113402.
3 A. Basem, S. Opakhai, Z. M. S. Elbarbary, F. Atamurotov and N. E. Benti, A comprehensive analysis of advanced solar panel productivity and efficiency through numerical models and emotional neural networks, *Sci. Rep.*, 2025, **15**(1), 259.
4 M. Mohammed, H. Aljibori, A. Al-Tamimi, Z. N. Alani, M. S. Hameed, F. M. Ibrahim, S. Al Jowder, A. Sharif and M. Alfiras, Toward sustainable smart cities in Bahrain: a groundbreaking approach to marine renewable energy harnessing sea tides and waves for a greener energy future, *2023 IEEE 8th International Conference on Engineering Technologies and Applied Sciences (ICETAS)*, IEEE, 2023, pp. 1–5.
5 Best Research-Cell Efficiency Chart, 2026. https://www.nrel.gov/pv/cell-efficiency.html.
6 S. Sidhik, I. Metcalf, W. Li, T. Kodalle, C. J. Dolan, M. Khalili, J. Hou, F. Mandani, A. Torma and H. Zhang, Two-dimensional perovskite templates for durable, efficient formamidinium perovskite solar cells, *Science*, 2024, **384**(6701), 1227–1235.
7 Z. Song, N. Meng, Y. Tian, J. Li, H. Ye, A. Mo, C. Sun, Z. Li, S. Yang and T. He, Halide insertion regulation for efficient and stable wide-bandgap perovskite photovoltaics, *Nat. Commun.*, 2025, **17**, 288.
8 J. Jeong, M. Kim, J. Seo, H. Lu, P. Ahlawat, A. Mishra, Y. Yang, M. A. Hope, F. T. Eickemeyer and M. Kim, Pseudo-halide anion engineering for α-FAPbI3 perovskite solar cells, *Nature*, 2021, **592**(7854), 381–385.
9 B.-T. Liu, H.-S. Su, I.-R. Chen, R.-H. Lee, Y.-F. Su, K.-T. Sun and S. Siddique, Dual-functional passivation on highly-efficient air-processed $FAPbI_3$ perovskite solar cells fabricated under high humidity without auxiliary equipment, *Appl. Surf. Sci. Adv.*, 2025, **25**, 100683.
10 J.-W. Lee, S.-G. Kim, S.-H. Bae, D.-K. Lee, O. Lin, Y. Yang and N.-G. Park, The interplay between trap density and hysteresis in planar heterojunction perovskite solar cells, *Nano Lett.*, 2017, **17**(7), 4270–4276.
11 Z. Yu, Z. Yang, Z. Ni, Y. Shao, B. Chen, Y. Lin, H. Wei, Z. J. Yu, Z. Holman and J. Huang, Simplified interconnection

structure based on C60/SnO2-x for all-perovskite tandem solar cells, *Nat. Energy*, 2020, **5**(9), 657–665.

12 S. Wang, D. Khan, W. Zhou, Y. Sui, T. Zhang, G. Yu, Y. Huang, X. Yang, X. Chen and H. Yan, Ion-Dipole Interaction for Self-Assembled Monolayers: A New Strategy for Buried Interface in Inverted Perovskite Solar Cells, *Adv. Funct. Mater.*, 2024, **34**(27), 2316202.

13 C. Xu, P. Hang, C. Kan, X. Guo, X. Song, C. Xu, G. You, W.-Q. Liao, H. Zhu and D. Wang, Molecular ferroelectric self-assembled interlayer for efficient perovskite solar cells, *Nat. Commun.*, 2025, **16**(1), 835.

14 L. Cao, Y. Tong, Y. Ke, W. Zhang, T. Li, Z. Kang, H. Wang and K. Wang, Modification of Nickel Oxide via Self-Assembled Monolayer for Enhanced Performance of Air-Processed FAPbI3 Perovskite Solar Cells, *ACS Appl. Energy Mater.*, 2024, **7**(4), 1508–1516.

15 Y. Zhang, T. Kong, Y. Liu, X. Liu, W. Liu, M. Saliba and D. Bi, The effect of self-assembled bridging layer on the performance of pure FAPbI3-based perovskite solar cells, *Adv. Funct. Mater.*, 2024, **34**(30), 2401391.

16 M. Kareem, B. Thaban, A. Rajiv, B. N. Sahu, S. Sundharam and P. Tomar, Multiscale simulation of eco-friendly perovskites under space radiation, *Nanoscale*, 2026, **18**(13), 7147–7163.

17 M. K. Hossain, M. H. K. Rubel, G. I. Toki, I. Alam, M. F. Rahman and H. Bencherif, Effect of various electron and hole transport layers on the performance of CsPbI3-based perovskite solar cells: a numerical investigation in DFT, SCAPS-1D, and wxAMPS frameworks, *ACS Omega*, 2022, **7**(47), 43210–43230.

18 J. Song, L. Qiu, C. Ding, S. Jin, J. Wang, K. Huang, H. Huang, J. Wu, R. Zhang and K. Sheng, Numerical simulation and performance optimization of all-inorganic CsGeI3 perovskite solar cells with stacked ETLs/C60 by SCAPS device simulation, *Mater. Today Commun.*, 2024, **38**, 108587.

19 M. Burgelman, P. Nollet and S. Degrave, Modelling polycrystalline semiconductor solar cells, *Thin Solid Films*, 2000, **361**, 527–532.

20 H. R. Abdul Ameer, A. N. Jarad, K. H. Salem, H. S. Hadi, M. A. Alkhafaji, R. S. Zabibah, K. A. Mohammed, K. Kumar Saxena, D. Buddhi and H. Singh, A role of back contact and temperature on the parameters of CdTe solar cell, *Adv. Mater. Process. Technol.*, 2024, **10**(2), 497–505.

21 Y. Tanaka, K. Ikegami, T. Maruyama, H. Kinjo and H. Ishii, Direct observation of charged state in C60-based field-effect transistor using operando photoelectron yield spectroscopy, *Appl. Phys. Express*, 2018, **11**(8), 081601.

22 Z. Chen, S. Jiang, X. Du, Y. Li, J. Shi, F. Tian, H. Wu, Y. Luo, D. Li and Q. Meng, Three-Dimensional (3D) Fluoride Molecular Glue to Improve the SnO2/Perovskite Interface for Efficient Perovskite Solar Cells, *Angew. Chem.*, 2025, **137**(3), e202415669.

23 W. Rehman, R. L. Milot, G. E. Eperon, C. Wehrenfennig, J. L. Boland, H. J. Snaith, M. B. Johnston and L. M. Herz, Charge-carrier dynamics and mobilities in formamidinium lead mixed-halide perovskites, *Adv. Mater.*, 2015, **27**(48), 7938–7944.

24 S. Park, J. H. Heo, C. H. Cheon, H. Kim, S. H. Im and H. J. Son, A [2, 2] paracyclophane triarylamine-based hole-transporting material for high performance perovskite solar cells, *J. Mater. Chem. A*, 2015, **3**(48), 24215–24220.

25 N. J. Jeon, H. G. Lee, Y. C. Kim, J. Seo, J. H. Noh, J. Lee and S. I. Seok, o-Methoxy substituents in spiro-OMeTAD for efficient inorganic–organic hybrid perovskite solar cells, *J. Am. Chem. Soc.*, 2014, **136**(22), 7837–7840.

26 H. Ashassi-Sorkhabi and P. Salehi-Abar, How the change of OMe substituent position affects the performance of spiro-OMeTAD in neutral and oxidized forms: theoretical approaches, *RSC Adv.*, 2018, **8**(33), 18234–18242.

27 M. K. A. Mohammed, Highly Efficient Perovskite Photovoltaics Enabled by Molecular Bridging at the SnO2/Perovskite Interface, *Langmuir*, 2025, **41**(26), 16960–16969.

28 M. Baro and P. Borgohain, Design and Performance Analysis of Perovskite Solar Cells: Insights from SCAPS 1D Device Simulations, *Renewable Energy*, 2025, 124225.

29 M. A. Green, *Solar Cells: Operating Principles, Technology, and System Applications*, 1982.

30 A. Riquelme, L. J. Bennett, N. E. Courtier, M. J. Wolf, L. Contreras-Bernal, A. B. Walker, G. Richardson and J. A. Anta, Identification of recombination losses and charge collection efficiency in a perovskite solar cell by comparing impedance response to a drift-diffusion model, *Nanoscale*, 2020, **12**(33), 17385–17398.

31 A. Mortadi, Y. Tabbai, E. El Hafidi, H. Nasrellah, E. Chahid, M. Monkade and R. El Moznine, Investigating temperature effects on perovskite solar cell performance via SCAPS-1D and impedance spectroscopy, *Clean Eng. Technol.*, 2025, **24**, 100876.

32 M. Y. H. Khan, S. S. Hasan, M. Z. Rahman, M. Rasheduzzaman and M. Z. Hasan, Enhancing perovskite solar cell performance using a BaSnS 3 chalcogenide perovskite: a device simulation study, *RSC Adv.*, 2025, **15**(41), 34643–34668.

33 M. Shah, I. Ahmad, J. Ullah, K. Hayat, M. Munawar, M. Mushtaq, A. Shah and S. K. Shah, First-Principles insights and SCAPS-1D simulations for optimizing MASnBr3-based perovskite solar cells, *Comput. Mater. Sci.*, 2025, **250**, 113699.

34 S. Wu, C. Li, S. Y. Lien and P. Gao, Temperature matters: enhancing performance and stability of perovskite solar cells through advanced annealing methods, *Chemistry*, 2024, **6**(1), 207–236.

35 H. Zhang, X. Qiao, Y. Shen and M. Wang, Effect of temperature on the efficiency of organometallic perovskite solar cells, *J. Energy Chem.*, 2015, **24**(6), 729–735.

36 D. Rueda-Delgado, I. M. Hossain, M. Jakoby, J. A. Schwenzer, T. Abzieher, I. A. Howard, B. S. Richards, U. Lemmer and U. W. Paetzold, Solution-processed and evaporated C60 interlayers for improved charge transport in perovskite photovoltaics, *Org. Electron.*, 2020, **77**, 105526.

37 L. Zuo, Z. Gu, T. Ye, W. Fu, G. Wu, H. Li and H. Chen, Enhanced photovoltaic performance of CH3NH3PbI3 perovskite solar cells through interfacial engineering using

self-assembling monolayer, *J. Am. Chem. Soc.*, 2015, **137**(7), 2674–2679.

38 G. George and S. Posada-Pérez, Interaction of C60 with methylammonium lead iodide perovskite surfaces: unveiling the role of C60 in surface engineering, *Chemistry–A European Journal*, 2024, **30**(38), e202401283.

39 G. Tumen-Ulzii, T. Matsushima, D. Klotz, M. R. Leyden, P. Wang, C. Qin, J.-W. Lee, S.-J. Lee, Y. Yang and C. Adachi, Hysteresis-less and stable perovskite solar cells with a self-assembled monolayer, *Commun. Mater.*, 2020, **1**(1), 31.

40 A. Kumar, M. Kaur, M. Atif, J. Kaur, R. Kaur, M. A. El-Meligy, P. Singh and M. Alhadrawi, Crystalline engineering of FAPbI 3 via pyrrolidinium ionic liquid for stable perovskite solar cells with 21.72% efficiency, *RSC Adv.*, 2024, **14**(46), 34027–34036.

41 A. Kumar, P. Sharma, A. Ved, J. Abd Hamid, A. I. Mohammed, A. Singh and V. Kaushik, Superior stabilized α-FAPbI3 perovskite solar cells with efficiency exceeding 24%, *Org. Electron.*, 2024, **135**, 107143.

42 Y. Meng, Y. Wang, C. Liu, P. Yan, K. Sun, Y. Wang, R. Tian, R. Cao, J. Zhu and H. Do, Epitaxial Growth of α-FAPbI3 at a Well-Matched Heterointerface for Efficient Perovskite Solar Cells and Solar Modules, *Adv. Mater.*, 2024, **36**(6), 2309208.

43 Y. Du, Q. Tian, S. Wang, L. Yin, C. Ma, Z. Wang, L. Lang, Y. Yang, K. Zhao and S. Liu, Crystallization control based on the regulation of solvent–perovskite coordination for high-performance ambient printable FAPbI3 perovskite solar cells, *Adv. Mater.*, 2024, **36**(9), 2307583.

44 Z. Xiong, L. Lan, Y. Wang, C. Lu, S. Qin, S. Chen, L. Zhou, C. Zhu, S. Li and L. Meng, Multifunctional polymer framework modified SnO2 enabling a photostable α-FAPbI3 perovskite solar cell with efficiency exceeding 23%, *ACS Energy Lett.*, 2021, **6**(11), 3824–3830.